

Electronic Supplementary Information for

Ligand-Free Sub-5 nm Platinum Nanocatalysts on Polydopamine Supports: Size-Controlled Synthesis and Size-Dictated Reaction Pathway Selection

*Wei Wang[†], Zixin Wang, Mengqi Sun, Hui Zhang[‡], and Hui Wang**

Department of Chemistry and Biochemistry, University of South Carolina, Columbia, South Carolina 29208, United States

** Corresponding author.*

Email: wang344@mailbox.sc.edu (H. Wang); Phone: 1-803-777-2203; Fax: 1-803-777-9521;
orcid.org/0000-0002-1874-5137.

[†] Permanent address: School of Chemistry and Materials Science, Nanjing University of Information Science & Technology, Nanjing, Jiangsu 210044, China

[‡] Permanent address: College of Chemistry and Materials Science, Nanjing Normal University, Nanjing, Jiangsu 210023, China

S1. Methods

S1.1 Chemicals and Materials

Anhydrous potassium hydroxide (KOH, granular) was purchased from J.T. Baker. Ethylene glycol (EG, Spectrophotometric grade, >99%) and isopropyl alcohol (GC Grade, >99.7%) were obtained from Alfa Aesar. Potassium tetrachloroplatinate (K_2PtCl_4 , reagent grade, 98%), dopamine hydrochloride ($C_8H_{11}NO_2$ HCl, 98%), tris base ($NH_2C(CH_2OH)_3$, $\geq 99.8\%$), ammonia borane (H_6BN , 97%), 4-nitrophenol ($C_6H_5NO_3$, 99%), Nafion perfluorinated resin solution (5 wt %), hydrochloric acid (HCl, 37%), palladium(II) chloride ($PdCl_2$, >99.9%), rhodium(III) chloride ($RhCl_3$, 98%), chloroauric acid ($HAuCl_4 \cdot 4H_2O$, >99.9%), and trizma base (TB, >99.0%) were purchased from Sigma-Aldrich. Ethanol (200 proof) and trisodium citrate dihydrate ($Na_3C_6H_5O_7 \cdot 2H_2O$, 99.0%) were purchased from Fisher Scientific. All reagents were used as received without further purification. Ultrapure water (18.2 M Ω resistivity, Barnstead EasyPure II 7138) was used for all experiments.

S1.2 Synthesis of Polydopamine (PDA) Nanoparticles

Colloidal PDA nanoparticles were synthesized through oxidative self-polymerization of dopamine at room temperature following a previously published protocol¹ with minor modifications. 100 mg of dopamine hydrochloride was dissolved in a mixture of 100 mL of Tris-buffer (10 mM tris base) and 40 mL of isopropyl alcohol with magnetic stirring at a speed of 400 rpm for 24 h at room temperature. The resulting PDA nanoparticles were collected by centrifuging the colloidal suspensions at 4400 rpm for 80 min, then washed/resuspended with water three times. The PDA nanoparticles were finally dispersed in 30 mL of water for future use.

S1.3 Synthesis of PDA-Supported Pt Nanocatalysts (PDA@Pt)

Pt nanocatalysts were deposited onto the surfaces of PDA colloids upon reduction of the Pt precursor, K_2PtCl_4 , under thermal conditions in EG, a polyol solvent with intrinsic temperature-dependent reducing capability,^{2, 3} without introducing any additional reducing agents. In a standard synthetic procedure, 50 μ L of colloidal PDA nanoparticles (containing 44.9 μ g of PDA) and x μ L (x = 2, 4, 6, 8, or 20) of 10 mM K_2PtCl_4 aqueous solution were introduced into 1 mL of EG preheated to 180 °C. The reactant mixtures were maintained at 180 °C in an oil bath for 20 min, and then rapidly cooled down in an ice bath. Under such synthetic conditions, EG served as both the solvent and a mild reducing agent for the Pt deposition.³ The as-synthesized PDA@Pt nanocatalysts were centrifuged at 4400 rpm for 40 min, then washed/resuspended with water three times, and finally dispersed in 1 mL of water. The samples synthesized at x values of 2, 4, 6, 8, and 20 were labeled as PDA@Pt-1, PDA@Pt-2, PDA@Pt-3, PDA@Pt-4, and PDA@Pt-5, respectively. The average size of the Pt nanoparticles on the PDA supports increased with the value of x. The reaction temperatures and the amount of K_2PtCl_4 precursors added to the reaction mixtures were both found to be key factors determining the sizes and morphologies of the Pt nanocatalysts deposited on the colloidal PDA supports.

S1.4 Structural Characterizations of PDA@Pt Nanocatalysts

The morphologies and structures of the PDA@Pt nanocatalysts were characterized by transmission electron microscopy (TEM) using a Hitachi H-8000 transmission electron microscope operated at an accelerating voltage of 200 kV. All samples for TEM measurements were dispersed in water and drop-dried on 300 mesh Formvar/carbon-coated Cu grids (Electron Microscopy Science Inc.). The compositions of the nanocatalysts were characterized by energy dispersive spectroscopy (EDS) using a Zeiss Ultraplus thermal field emission scanning electron microscope. The samples for EDS measurements were dispersed in water and drop-dried on silicon wafers (UniversityWafer, Inc.). Powder X-ray diffraction (PXRD) patterns were recorded on a SAXSLab Ganesha at the South Carolina SAXS Collaborative (Cu K α = 1.5406 Å).

S1.5 Measurements of Electrochemical Surface Areas (ECSAs) of Pt

Cyclic voltammetry (CV) measurements were performed on a CHI 660E electrochemistry workstation (CH Instruments, Austin, Texas) at room temperature with a three-electrode system composed of a Pt wire as the auxiliary, a saturated calomel electrode (SCE) as the reference, and a nanocatalyst-loaded glassy carbon electrode (GCE, 3 mm diameter) as the working electrode. Typically, the GCE was polished with 0.3 mm alumina slurry, followed by washing with water and ethanol. 8 μ L of PDA@Pt colloidal ink was drop-casted on a pretreated GCE and dried in air at room temperature. Then 2 μ L of Nafion solution (0.2 wt %) was drop-dried on the electrode surface to hold the PDA@Pt nanocatalysts. To measure the ECSAs of Pt, CV measurements were performed in N₂-purged 0.5 M H₂SO₄ aqueous solution at a potential sweep rate of 50 mV s⁻¹ from -0.3 V to 0.5 V (vs. SCE). The polarization trace was normalized against the mass of Pt in the nanocatalysts on each electrode, which was calculated based on the PDA mass on each electrode and the Pt/PDA mass ratios quantified by EDS. During the anodic potential sweep, the oxidation peaks in the potential ranges of -0.3–0 V were the electrochemical signatures of the hydrogen underpotential desorption from Pt surfaces. During the cathodic potential sweep, the sharp increase in the reduction current below -0.2 V signified the Pt-catalyzed hydrogen evolution. The mass-specific ECSAs of Pt on various nanocatalysts were calculated on the basis of the areas of the hydrogen underpotential desorption peaks, assuming that the specific charge associated with hydrogen desorption from the Pt surfaces was 210 μ C cm⁻².⁴ Assuming a spherical shape of the Pt nanocatalysts, the theoretical values of the mass-specific surface areas (SA_{ms}) of Pt were calculated using the following equation:

$$SA_{ms}(Pt) = \frac{4\pi \times r^2}{\frac{4}{3}\pi \times r^3 \times \rho} = \frac{3}{r \times \rho} \quad (\text{Equation. S1}),$$

where r and ρ are the radius of Pt nanoparticles (obtained from TEM analysis) and the density of Pt (21.45 g/cm³), respectively. The percentages of the active Pt surface area (active S_{Pt} %) were further calculated by normalizing the experimentally measured mass-specific ECSAs against the theoretical mass-specific surface areas of Pt.

S1.6 Analysis of the Kinetic Results

The catalytic transfer hydrogenation of NP by AB⁵⁻⁸ was selected as a model reaction to investigate the size-dependent multimodal catalytic behaviors of the PDA@Pt nanocatalysts. In a basic aqueous environment, NP existed in the form of 4-nitrophenolate, which exhibited a strong absorption peak at ~400 nm whose intensity gradually decreased as the hydrogenation reaction proceeded. Meanwhile, another absorption peak centered at 310 nm emerged and became progressively more intense during the reactions, signifying the formation of 4-aminophenol (AP), the product of the hydrogenation reactions. The reaction kinetics could be monitored in real time by tracking the temporal evolution of the absorbance at the wavelength of either 400 or 310 nm during the reactions. The fraction of NP (θ_{NP}) was equal to the ratio between NP concentration (C_{NP}) and the initial concentration of NP ($C_{NP,0}$). According to the Lambert-Beer law, C_{NP} was proportional to the absorbance (A) at 400 nm. Therefore, θ_{NP} could be calculated by normalizing A against the initial absorbance (A_0) at the wavelength of 400 nm:

$$\theta_{NP} = \frac{C_{NP}}{C_{NP,0}} = \frac{A(at\ 400nm)}{A_0(at\ 400nm)} \quad (\text{Equation S2}).$$

Similarly, the fraction of AP (θ_{AP}) could be calculated based on the absorbance at 310 nm using the following equation:

$$\theta_{AP} = \frac{C_{AP}}{C_{AP,t=\infty}} = \frac{A(at\ 310nm)}{A_{t=\infty}(at\ 310nm)} \quad (\text{Equation S3}),$$

where $C_{AP,t=\infty}$ and $A_{t=\infty}$ refer to the AP concentration and absorbance, respectively, at an infinitely long reaction time after all the NP molecules were fully converted into AP.

At the initial stage of the reaction, there was an induction time (t_{ind}) during which θ_{NP} remained unchanged without producing AP at any detectable level. When AB was in large excess with respect to NP ($C_{AB,0} \gg C_{NP,0}$), the concentration of AB (C_{AB}) remained essentially constant at its initial value, $C_{AB,0}$, during the catalytic reactions. Once the NP-to-AP conversion was initiated, the temporal evolution of θ_{NP} and θ_{AP} obeyed a pseudo-first-order rate law until approaching complete consumption of NP, which could be described by the following rate equations:

$$-\ln(\theta_{NP}) = k_{obs} \times (t - t_{ind}) \quad (\text{Equation S4}),$$

$$\text{and } -\ln(1 - \theta_{AP}) = k_{obs} \times (t - t_{ind}) \quad (\text{Equation S5}).$$

Equations S4 and S5 are the integral forms of the rate law describing the consumption of NP and the production of AP, respectively. k_{obs} is the apparent pseudo-first-order rate constant, which could be obtained by fitting the experimentally measured kinetic results using Equation S4 or S5.

S1.7 Langmuir-Hinshelwood (LH) and Eley-Rideal (ER) Mechanisms

In the LH mechanism, the bimolecular reaction occurs between an NP and an AB molecule that are both adsorbed on the Pt nanocatalyst surfaces. Both NP and AB compete for the active sites on the nanocatalyst surfaces through Langmuir adsorption. The derivative form of the rate law can be described by the following equation:

$$-\frac{dC_{NP}}{dt} = kQ_{NP}Q_{AB} = \frac{kS^2K_{AB}C_{AB}K_{NP}C_{NP}}{(1 + K_{AB}C_{AB} + K_{NP}C_{NP})^2} \quad (\text{Equation S6}),$$

where Q_{NP} and Q_{AB} refer to the surface coverages of NP and AB, respectively. k is the second order rate constant. S is the total active surface area of the catalysts. K_{NP} and K_{AB} are the equilibrium constants for NP and AB adsorption, respectively.

The rate constant at the initial stage of an LH reaction is related to a series of kinetic and thermodynamic parameters as described by the following equation:

$$k_{obs, LH} = \frac{kS^2K_{AB}C_{AB,0}K_{NP}}{(1 + K_{AB}C_{AB,0} + K_{NP}C_{NP,0})^2} \quad (\text{Equation S7}),$$

in which $k_{obs, LH}$ is the experimentally observed rate constant at the initial stage of an LH reaction. The value of $-\ln(\theta_{NP})$ varies linearly with the reaction time (first-order kinetics), t , at the early stage of an LH reaction, and deviates from the first-order kinetics at later stages of the reactions after a significant fraction of AB has been consumed. Therefore, the values of $k_{obs, LH}$ can be obtained by fitting the linear part of the temporally evolving curves of $-\ln(\theta_{NP})$ at the early stage of the reactions using the Equation S4. When AB is in large excess with respect to NP, $K_{AB}C_{AB}$ becomes far greater than $K_{NP}C_{NP}$ and C_{AB} is maintained very close to $C_{AB,0}$ throughout the entire process. Under these conditions, the reaction obeys first-order kinetics until approaching completion, and $k_{obs, LH}$ becomes essentially equivalent to the experimentally determined pseudo-first-order rate constant, as shown in the following equation:

$$k_{obs, LH} = \frac{kS^2K_{AB}C_{AB}K_{NP}}{(1 + K_{AB}C_{AB} + K_{NP}C_{NP})^2} \approx \frac{kS^2K_{AB}C_{AB,0}K_{NP}}{(1 + K_{AB}C_{AB,0})^2} \approx \frac{kS^2K_{AB}C_{AB,0}K_{NP}}{(1 + K_{AB}C_{AB,0} + K_{NP}C_{NP,0})^2} \quad (\text{Equation S8}).$$

The ER mechanism involves the bimolecular reaction between a surface-adsorbed AB molecule and an NP molecule from the solution phase at the solution/catalyst interface. The reaction rate is proportional to the surface coverage of AB and the concentration of NP, as described by the following rate law in its derivative form:

$$k_{obs, ER} = \frac{k'SK_{AB}C_{AB}}{1 + K_{AB}C_{AB} + K_{NP}C_{NP}} \quad (\text{Equation S9}),$$

where k' is the intrinsic turn-over rate at each active surface site for an ER reaction.

Analogous to the LH reactions, an ER reaction also obeys first-order kinetics at its initial stage. The initial rate constant, $k_{obs, ER}$, can be obtained by fitting the linear part of the $-\ln(\theta_{NP})$ trajectories at the early stage of the reactions:

$$k_{obs, ER} \approx \frac{k'SK_{AB}C_{AB,0}}{1 + K_{AB}C_{AB,0} + K_{NP}C_{NP,0}} \quad (\text{Equation S10}).$$

When $C_{AB,0} \gg C_{NP,0}$, the surface coverage of AB remained unchanged throughout the entire reaction. As a result, the reaction obeys first-order kinetics, with the values of $-\ln(\theta_{NP})$ evolving linearly over time. Because the Pt surfaces are predominately occupied by AB ($Q_{AB} \gg Q_{NP}$), the equation for $k_{obs, ER}$ can be further simplified as follows:

$$k_{obs,ER} \approx \frac{k'SK_{AB}C_{AB,0}}{1 + K_{AB}C_{AB,0}} \quad (\text{Equation S11}).$$

Under our experimental conditions, the rates of both the LH and ER reactions could be well-described by the pseudo-first order kinetics and we were unable to distinguish the two mechanisms simply based on the values of the rate constants. However, as shown by Equations S8 and S11, the rate constants for the LH and ER mechanisms, $k_{obs,HL}$ and $k_{obs,ER}$, depend very differently on the total active Pt surface area, S , which is directly proportional to the volume of PDA@Pt nanocatalyst particles added to the reaction mixtures for a given catalyst sample. We plotted k_{obs} as a function of the volume of colloidal PDA@Pt nanocatalysts (V) added into the reactant mixtures and fitted the experimental results with the following equation:

$$k_{obs} = \alpha \times V^n \quad (\text{Equation S12}),$$

where α is a fractional constant, which relates the experimentally determined k_{obs} to the n^{th} power of V . For an ER reaction, k_{obs} varies linearly with V , whereas the k_{obs} for an LH reaction is proportional to V^2 .

At a fixed $C_{NP,0}$, $k_{obs,HL}$ and $k_{obs,ER}$ also exhibit different evolutionary profiles as the $C_{AB,0}$ varies. While $k_{obs,ER}$ increases monotonically with $C_{AB,0}$ following the same trend as the Langmuir adsorption isotherm of AB, $k_{obs,LH}$ holds a volcano-type relationship to the $C_{AB,0}$ as a consequence of competitive adsorption of NP and AB on the Pt nanocatalyst surfaces. By fitting the plots of $k_{obs,LH}$ vs. $C_{AB,0}$, the values of K_{AB} and K_{NP} can be obtained, which will allow us to evaluate the relative adsorption affinities of NP and AB to the surfaces of size-controlled Pt nanocatalysts. We observed that the catalytic transfer hydrogenation of NP by AB switched from the LH to the ER mechanism as the size of Pt nanoparticles increased from 1.7 nm to 4.6 nm at a pH of 12. At intermediate particle sizes around 4 nm, the reaction occurred through both the LH and ER mechanisms concurrently. As a consequence, the overall rate constants were essentially the sum of $k_{obs,HL}$ and $k_{obs,ER}$ as described by the following equation:

$$k_{obs} = k_{obs,LH} + k_{obs,ER} = \frac{K_{AB}C_{AB,0}K_{NP}}{(1 + K_{AB}C_{AB,0} + K_{NP}C_{NP,0})^2}kS^2 + \frac{K_{AB}C_{AB,0}}{1 + K_{AB}C_{AB,0}}k'S \quad (\text{Equation S13}),$$

where the relative values of kS^2 and $k'S$ reflect the relative contributions of the LH and the ER components to the overall reaction kinetics. Equation S13 was used to fit the kinetic results collected from the PDA@Pt-4 nanocatalysts, adapting the values of the equilibrium constants obtained from PDA@Pt-3 and PDA@Pt-5 nanocatalysts, respectively.

S1.8 Synthesis of PDA-Supported Rh and Pd Nanocatalysts

PDA-supported Rh (PDA@Rh) and Pd (PDA@Pd) nanocatalysts were synthesized following a similar procedure using H_2PdCl_4 and $RhCl_3$ as the metal precursors, respectively. To synthesize PDA@Rh nanocatalysts, 200 μL of PDA nanoparticles and 30 μL of 10 mM $RhCl_3$ aqueous solution were added into 1 mL of EG preheated to 180 $^\circ\text{C}$. The reactant mixtures were then maintained at 180 $^\circ\text{C}$ in an oil bath for 20 min before cooling down to room temperature. To synthesize PDA@Pd nanocatalysts, 200 μL of PDA nanoparticles and 25 μL of 10 mM H_2PdCl_4 aqueous solution (prepared by mixing $PdCl_2$ and HCl at a

molar ratio of 1:2) were added into 1 mL of EG preheated to 180 °C. The reactant mixtures were then maintained at 180 °C in an oil bath for 20 min before cooling down to room temperature. The as-synthesized PDA@Rh and PDA@Pd nanocatalysts were centrifuged at 4400 rpm for 40 min, then washed/resuspended with water three times, and finally dispersed in 1 mL of water.

S1.9 Synthesis of Pt Nanocatalysts on Au@PDA Core-Shell Supports

Quasi-spherical Au nanoparticles were synthesized using a previously reported seed-mediated overgrowth method.⁹ First, colloidal Au seeds with an average size of 17 nm were synthesized by reducing HAuCl₄ with citrate in aqueous solution. Briefly, 0.5 mL of 0.25 mM HAuCl₄ aqueous solution was first added into 48 ml of boiling H₂O under magnetic stir. After reflux for 10 minutes, 1.5 mL of 1 wt % trisodium citrate aqueous solution was rapidly injected into the reactant solution. The reaction solution was further refluxed for 30 min under magnetic stir, and then cooled to room temperature for further use.

Au nanoparticles with an average diameter of ~48 nm were synthesized by boiling a mixture of 180 mL water and 8 mL of 0.1 M TB aqueous solution with magnetic stir for 10 min. Then, 8 mL of the as-synthesized colloidal Au seeds and 4 mL of 25 mM HAuCl₄ solution were successively added to a boiling TB solution, followed by further reflux for 30 min under magnetic stir. The resulting Au nanoparticles were centrifuged at 1000 rpm for 20 min, then washed/resuspended with water twice, and finally dispersed in 200 mL of water. A second seed-mediated growth step led to the formation of larger Au nanoparticles with an average diameter of ~116 nm, which were synthesized by boiling a mixture of 91.5 mL water, 2 mL TB (0.1 M) solution, 6 mL of Au nanoparticles (~ 48 nm in diameter), and 0.5 mL of HAuCl₄ (25 mM) for 30 min under magnetic stir at 400 rpm. The resulting Au colloids were centrifuged and redispersed in 100 mL of water for storage.

Au@PDA core-shell nanoparticles were synthesized by stirring a mixture containing 4 mL of colloidal Au nanoparticles (~ 116 nm in diameter), 10 mL of 0.1 M TB, and 4 mL of isopropyl alcohol at room temperature for 24 hours. The resulting Au@PDA core-shell nanoparticles were collected through centrifugation and re-dispersion in H₂O twice and finally dispersed in 1 mL of H₂O. The as-synthesized Au@PDA core-shell nanoparticles were about the same size as the PDA nanoparticles with an average outer diameter of ~ 168 nm.

To synthesize Pt nanocatalysts on Au@PDA core-shell supports, 50 µL of Au@PDA core-shell nanoparticles and 4 µL of 10 mM K₂PtCl₄ aqueous solution were added into 1 mL of EG preheated to 180 °C. The reactant mixtures were then maintained at 180 °C in an oil bath for 20 min. The as-synthesized Au@PDA@Pt nanoparticles were centrifuged at 1000 rpm for 20 min, then washed/resuspended with water three times, and finally dispersed in 1 mL of water.

S2. Additional Figures

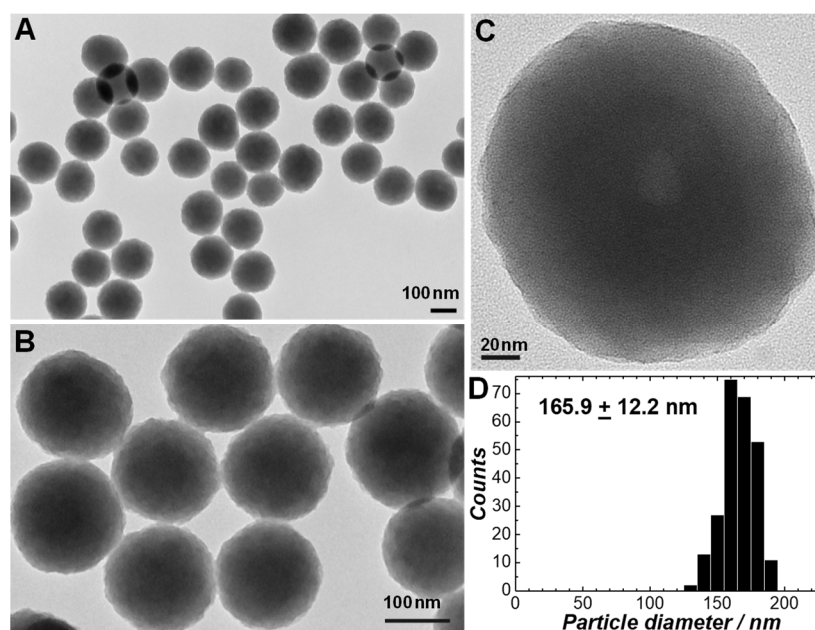


Figure S1. (A, B, C) TEM images taken at various magnifications and (D) size distribution of PDA nanoparticles. The analysis of particle sizes was conducted using the Image J Software.

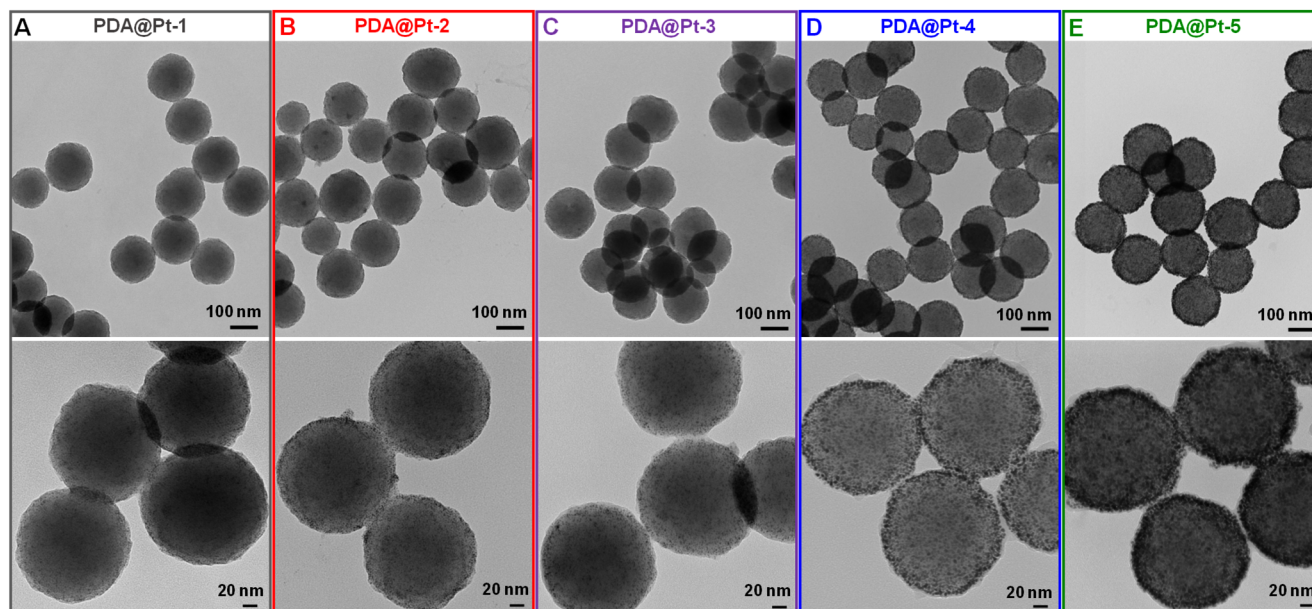


Figure S2. TEM images of (A) PDA@Pt-1, (B) PDA@Pt-2, (C) PDA@Pt-3, (D) PDA@Pt-4, and (E) PDA@Pt-5 nanocatalysts, which were synthesized by adding x μL of 10 mM K_2PtCl_4 into the reactant mixtures ($x = 2, 4, 6, 8,$ and 20 for PDA@Pt-1, PDA@Pt-2, PDA@Pt-3, PDA@Pt-4, and PDA@Pt-5, respectively). TEM images in the upper row were taken at a lower magnification than those in the lower row. Higher-magnification TEM images highlighting more detailed structural features of individual PDA@Pt particles were shown in Figure 1.

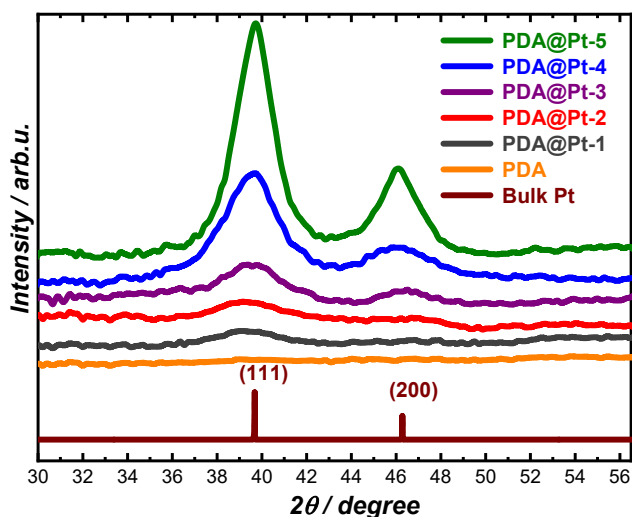


Figure S3. Powder X-ray diffraction (PXRD) patterns of PDA nanoparticles and various PDA@Pt nanocatalysts. The PXRD patterns are offset for clarity. The standard diffraction pattern of face-centered cubic (fcc) phase of bulk Pt (JCPDS Card No. 1-1190) is shown at the bottom as the reference.

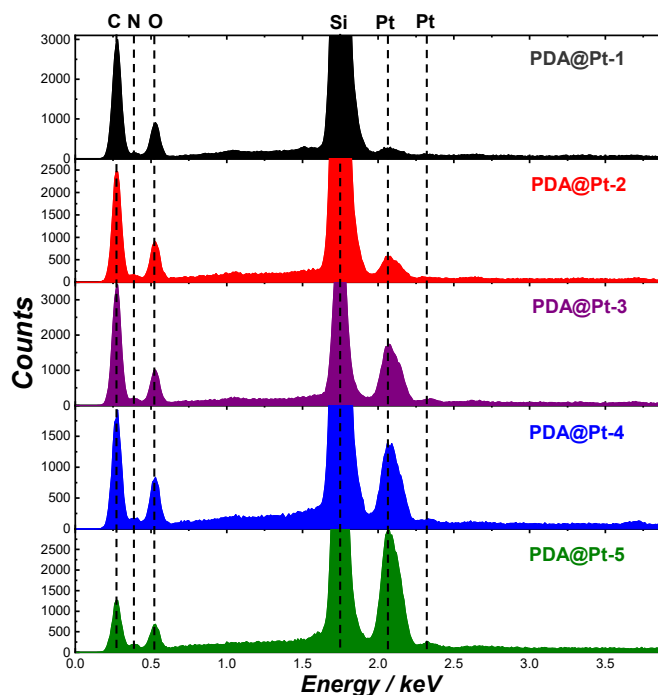


Figure S4. Energy dispersive spectra (EDS) of PDA@Pt-1, PDA@Pt-2, PDA@Pt-3, PDA@Pt-4, and PDA@Pt-5 nanocatalysts. The signals of C, N, O, and Pt elements were all well-resolved. The Si signals originated from the Si substrates. The atomic ratio of N:C:O was measured to be 1: 8.2: 2.1, which was in good agreement with the chemical formulars of dopamine and PDA. The Pt/PDA mass ratios were quantified based on the relative intensities of the Pt signals to those of the sum of C, N, and O signals in the EDS.

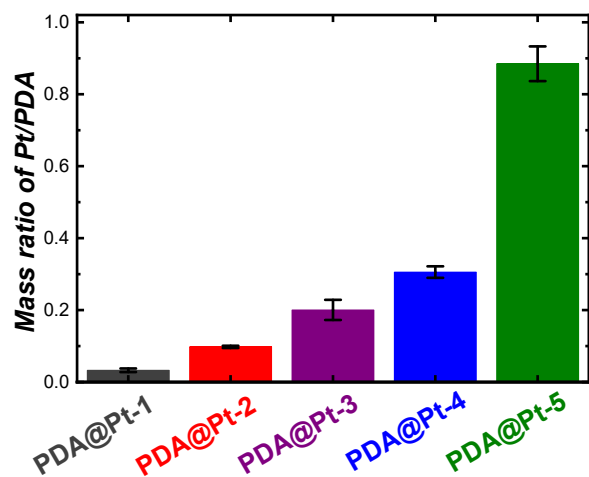


Figure S5. Pt/PDA mass ratios of PDA@Pt-1, PDA@Pt-2, PDA@Pt-3, PDA@Pt-4, and PDA@Pt-5 nanocatalysts calculated based on the EDS results. The error bars represent the standard deviations of EDS results collected from three different regions in each sample.

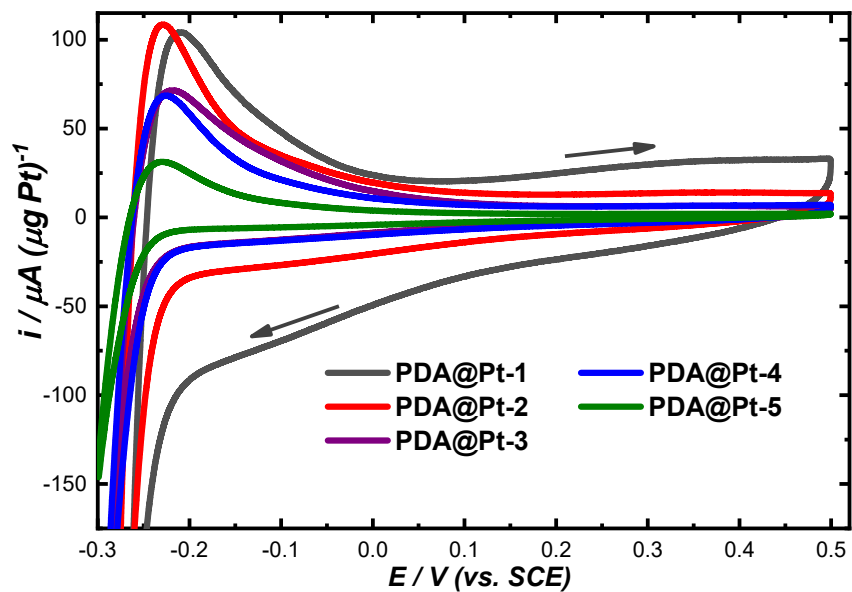


Figure S6. Cyclic voltammetry (CV) curves of PDA@Pt nanocatalysts in an aqueous electrolyte containing 0.5 M H_2SO_4 at a potential sweep rate of 50 mV s^{-1} . The kinetic currents were normalized against the mass of Pt in the PDA@Pt nanocatalysts loaded on each electrode.

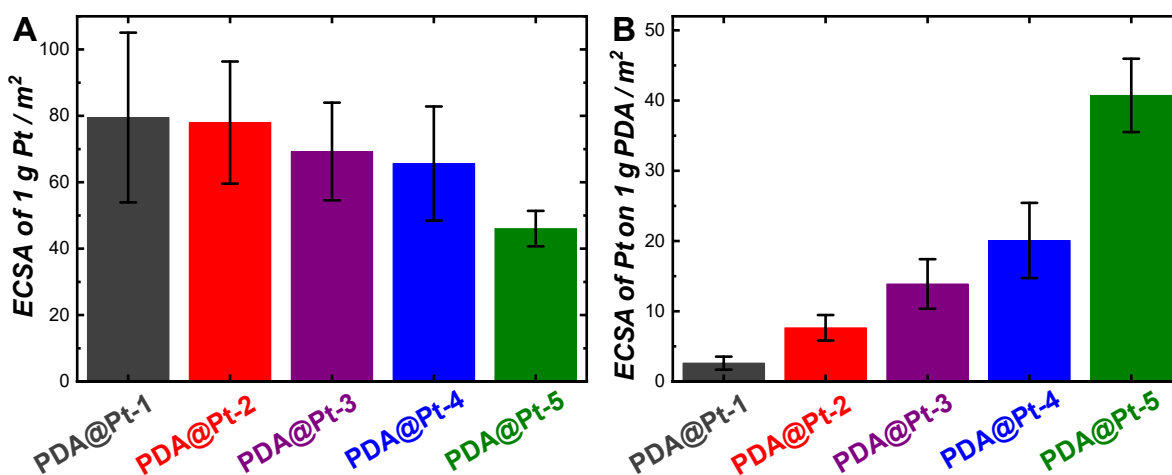


Figure S7. (A) Mass-specific ECSAs of Pt and (B) ECSAs of Pt on 1 g PDA for various PDA@Pt nanocatalysts calculated based on the areas of the hydrogen underpotential desorption peaks in CV curves. The error bars in the inset represent the standard deviations of the results collected from three PDA@Pt-loaded electrodes.

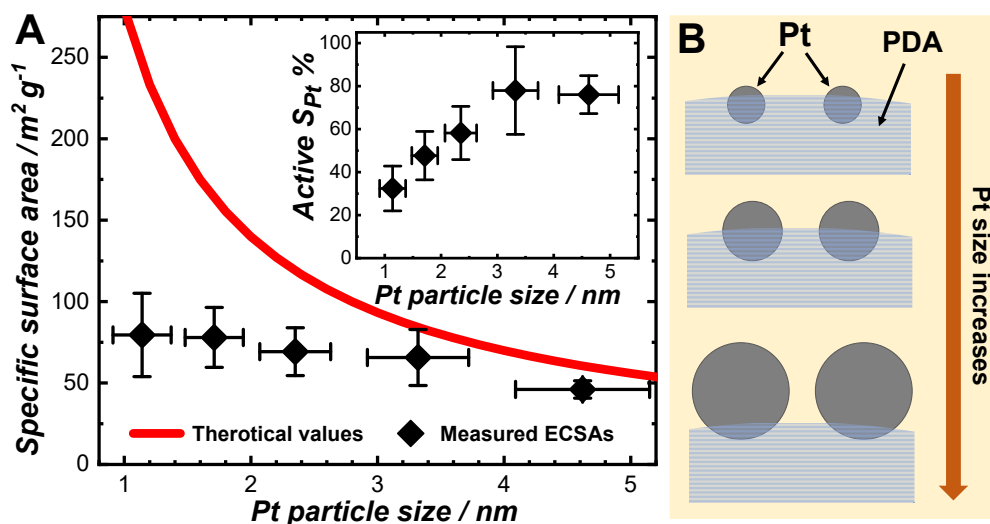


Figure S8. (A) Calculated mass-specific surface areas (red line) and experimentally measured mass-specific ECSAs of PDA@Pt nanocatalysts as a function of Pt particle size. The inset shows the relationship between the percentage of active Pt surface area (S_{Pt} %) and the Pt particle size. The values of active S_{Pt} % were calculated by normalizing the experimentally measured mass-specific ECSAs against the theoretical mass-specific surface areas of Pt. (B) Cartoons illustrating the cross-sectional view of the geometry of the PDA@Pt nanocatalysts, in which each Pt nanoparticle is partially embedded in the PDA support.

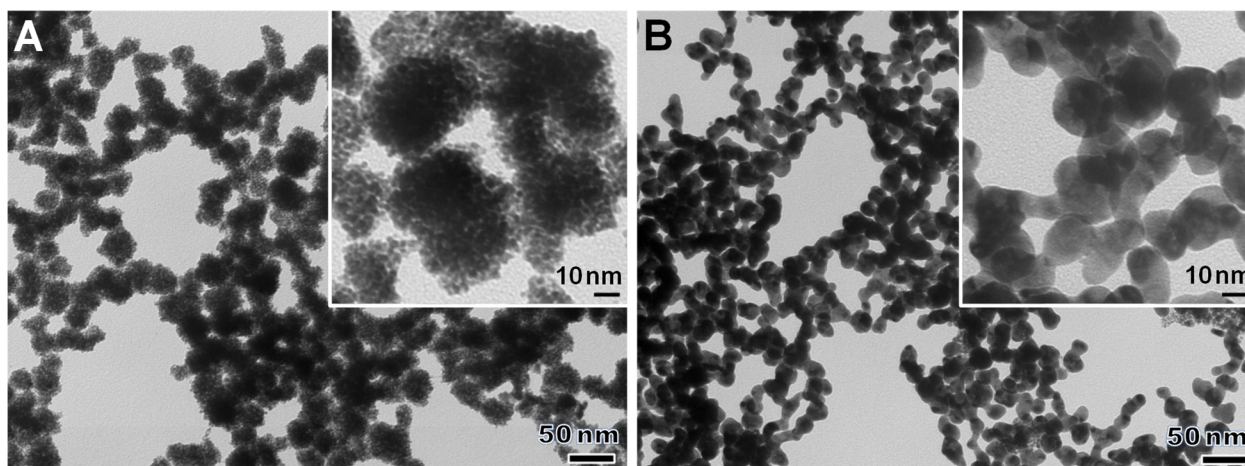


Figure S9. TEM images of Pt nanoparticles synthesized after maintaining 1 mL of 80 μM K_2PtCl_4 in EG at (A) 120 and (B) 180 $^\circ\text{C}$ for 3 h in the absence of PDA supports. Higher-magnification TEM images are shown in the insets.

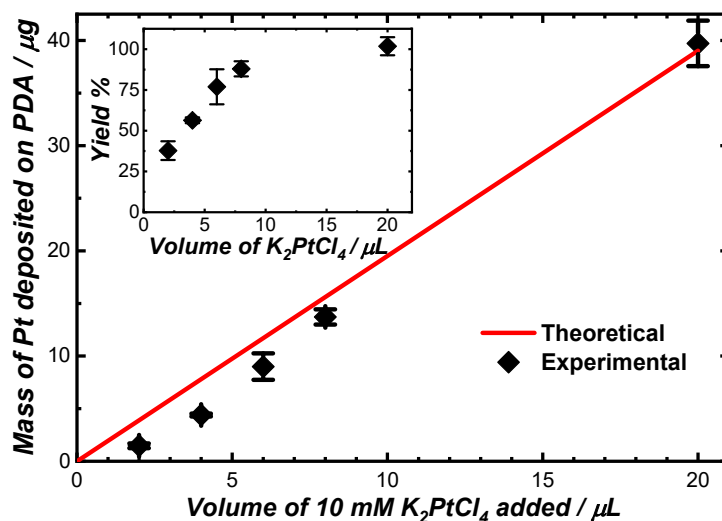


Figure S10. Relationship between mass of Pt deposited on PDA and the volume of 10 mM K_2PtCl_4 added to the reactant mixtures. The PDA@Pt nanocatalysts were synthesized by reacting 44.5 μg PDA with various volumes of 10 mM K_2PtCl_4 in 1 mL of EG at 180 $^\circ\text{C}$ for 20 min. The black diamonds represent the experimental results quantified by EDS and the solid red line represent the theoretical values of total Pt mass in the K_2PtCl_4 precursor. The inset shows relationship between yield of Pt deposition on PDA and the volume of 10 mM K_2PtCl_4 added to the reactant mixtures. The yields of Pt deposition were calculated by normalizing the experimentally measured mass of Pt deposited on PDA against the theoretical values of total mass of Pt in the K_2PtCl_4 precursor.

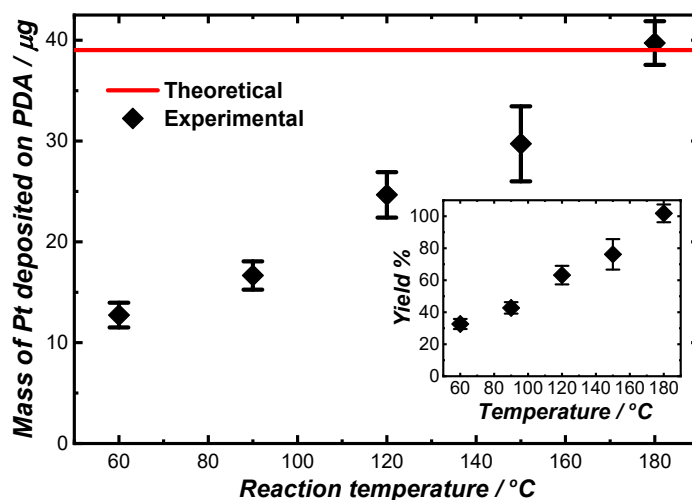


Figure S11. Relationship between mass of Pt deposited on PDA and the reaction temperature. The PDA@Pt nanocatalysts were synthesized by reacting 44.5 µg PDA with 20 µL of 10 mM K_2PtCl_4 in 1 mL of EG at various temperatures for 20 min. volume of 10 mM K_2PtCl_4 added to the reactant mixtures. The black diamonds represent the experimental results quantified by EDS and the solid red line represent the theoretical values of total Pt mass in the K_2PtCl_4 precursor. The inset shows relationship between yield of Pt deposition on PDA and the reaction temperature. The yields of Pt deposition were calculated by normalizing the experimentally measured mass of Pt deposited on PDA against the theoretical values of total mass of Pt in the K_2PtCl_4 precursor.

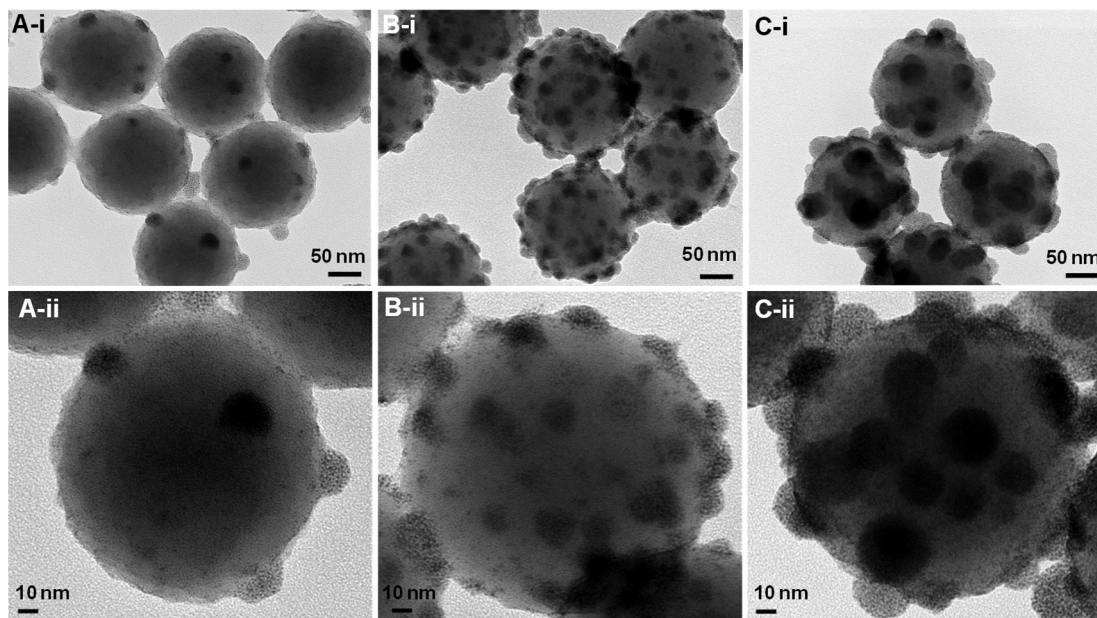


Figure S12. TEM images of PDA@Pt nanocatalysts synthesized by reacting 44.5 µg PDA nanoparticles with (A) 4 µL, (B) 20 µL, and (C) 100 µL of 10 mM K_2PtCl_4 1 mL EG at a reaction temperature of 60 °C for 20 min. The TEM images in panels i have a higher magnification than those in panels ii.

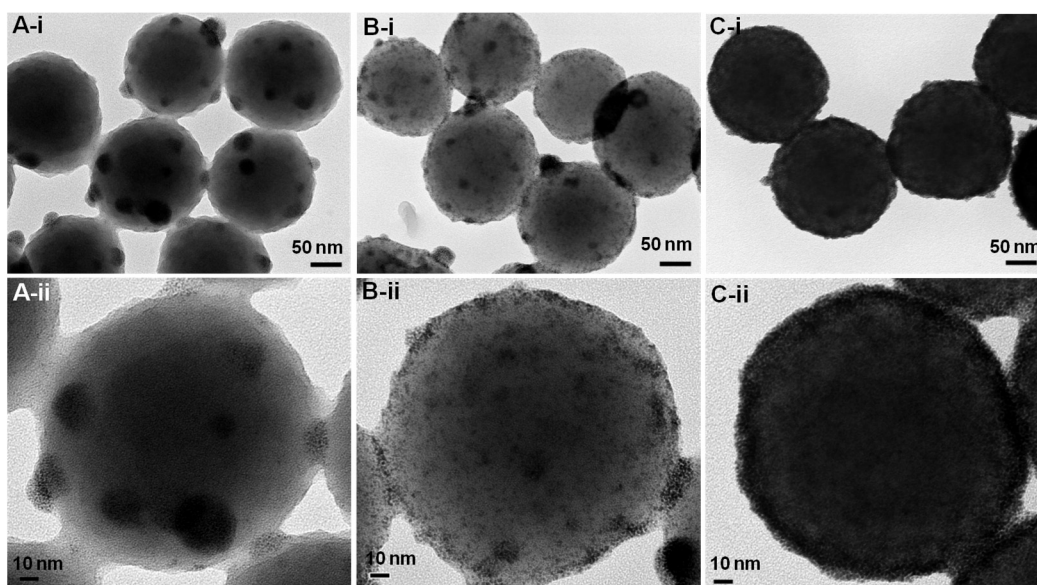


Figure S13. TEM images of PDA@Pt nanocatalysts synthesized by reacting 44.5 μg PDA nanoparticles with (A) 4 μL , (B) 20 μL , and (C) 100 μL of 10 mM K_2PtCl_4 1 mL EG at a reaction temperature of 90 $^\circ\text{C}$ for 20 min. The TEM images in panels i have a higher magnification than those in panels ii.

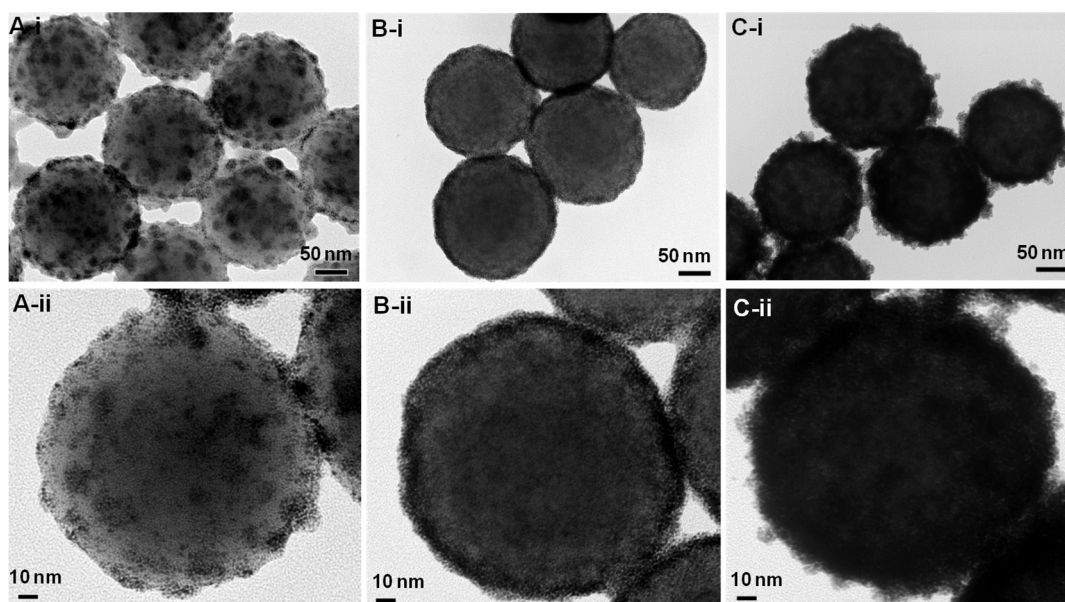


Figure S14. TEM images of PDA@Pt nanocatalysts synthesized by reacting 44.5 μg PDA nanoparticles with (A) 4 μL , (B) 20 μL , and (C) 100 μL of 10 mM K_2PtCl_4 1 mL EG at a reaction temperature of 120 $^\circ\text{C}$ for 20 min. The TEM images in panels i have a higher magnification than those in panels ii.

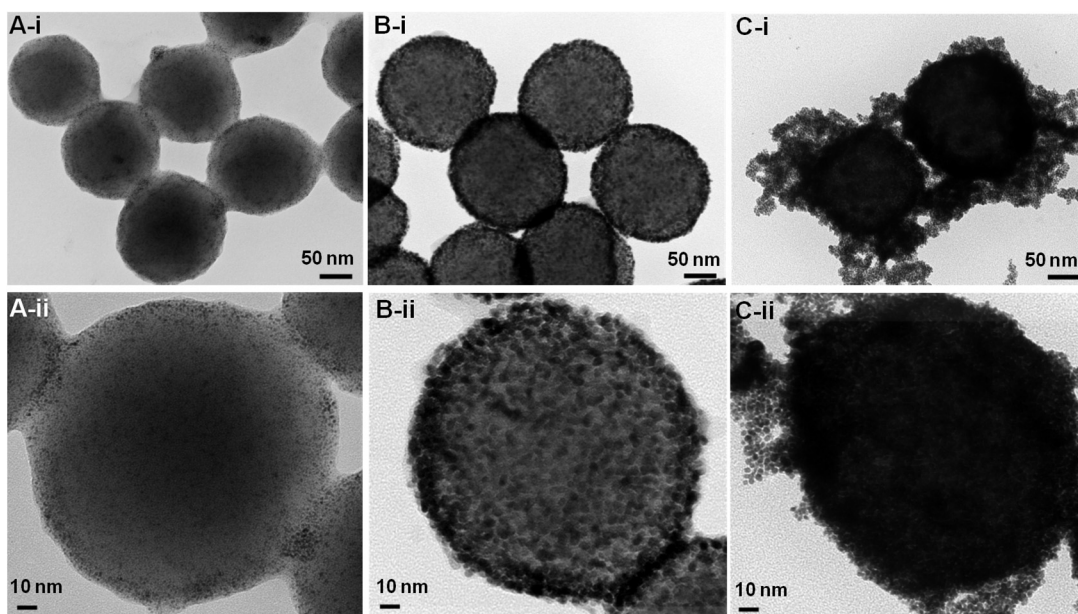


Figure S15. TEM images of PDA@Pt nanocatalysts synthesized by reacting 44.5 μg PDA nanoparticles with (A) 4 μL , (B) 20 μL , and (C) 100 μL of 10 mM K_2PtCl_4 1 mL EG at a reaction temperature of 150 $^\circ\text{C}$ for 20 min. The TEM images in panels i have a higher magnification than those in panels ii.

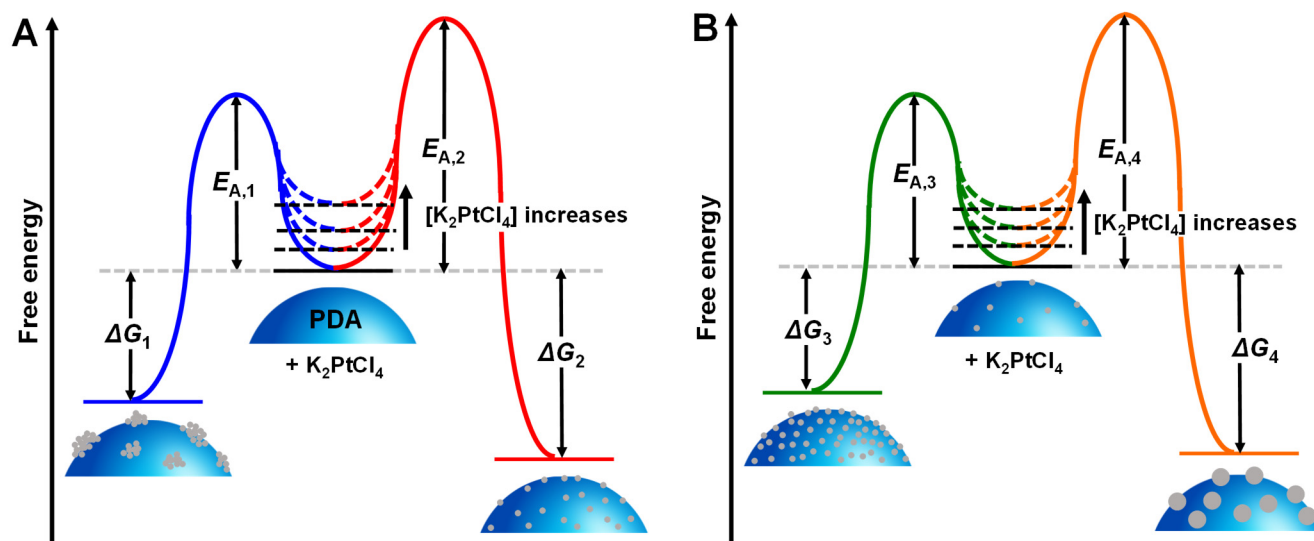


Figure S16. (A) Potential energy diagram illustrating the selective formation of clustered Pt islands vs. well-dispersed Pt nanoparticles on the PDA surfaces. (B) Potential energy diagram illustrating the activation energy barriers for Pt nucleation vs. Pt nanocrystal growth on the PDA surfaces. The ΔG s and E_{AS} refer to the free energy changes and activation energy barriers, respectively.

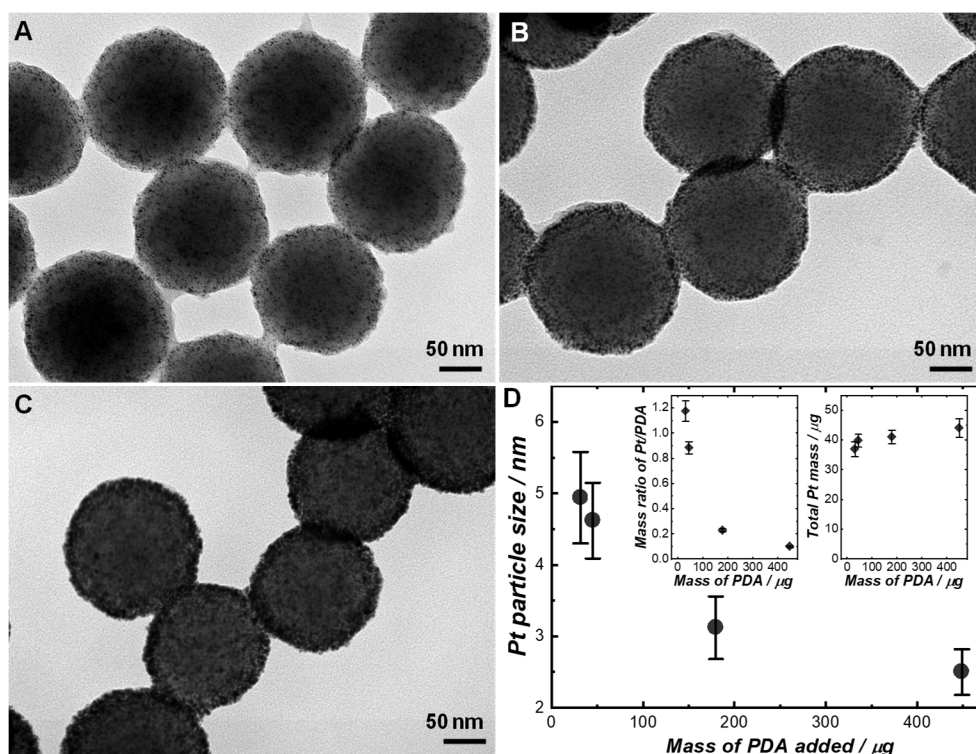


Figure S17. TEM images of PDA@Pt NPs synthesized in 1 mL of EG containing 20 μL of 10 mM K_2PtCl_4 and (A) 500 μL , (B) (A) 200 μL , and (C) 35 μL of PDA nanoparticles at 180 $^\circ\text{C}$. (D) Relationship between Pt particle sizes and mass of PDA added in the reactant mixtures. The insets show the evolutions of Pt/PDA mass ratios and total Pt mass deposited on PDA upon variation of the mass of PDA added to the reactant mixtures.

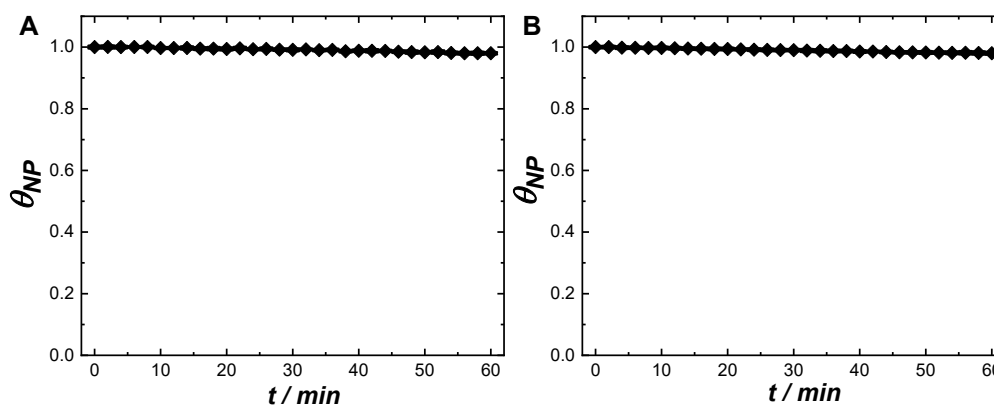


Figure S18. Temporal evolution of the fraction of NP (θ_{NP}) during catalytic hydrogenation reactions at room temperature after mixing AB with NP (A) in the absence of any nanocatalysts and (B) in the presence of 1.35 μg PDA nanoparticles. The initial concentrations of NP, AB, and KOH were 56 μM , 5.6 mM, and 10 mM, respectively. The total volume of the reactant mixtures was kept at 1.8 mL. The error bars in the panels represent the standard deviations obtained from three experimental runs under identical reaction conditions.

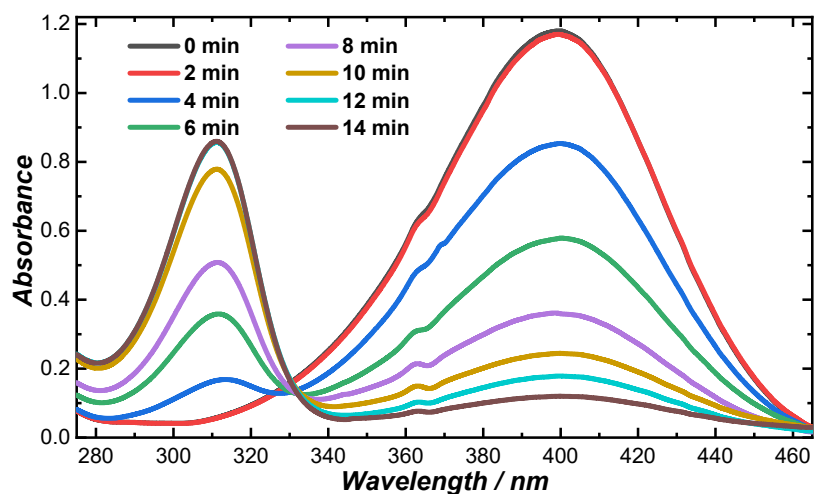


Figure S19. UV-vis absorption spectra during the catalytic reactions. $C_{NP,0}$, $C_{AB,0}$, and $C_{KOH,0}$ were kept at $56 \mu\text{M}$, 5.6 mM , and 10 mM , respectively, with $30 \mu\text{L}$ of colloidal PDA@Pt-2 nanocatalysts (containing $44.9 \mu\text{g mL}^{-1}$ PDA) added to the reactant mixtures. The total volume of the reactant mixtures was 1.8 mL .

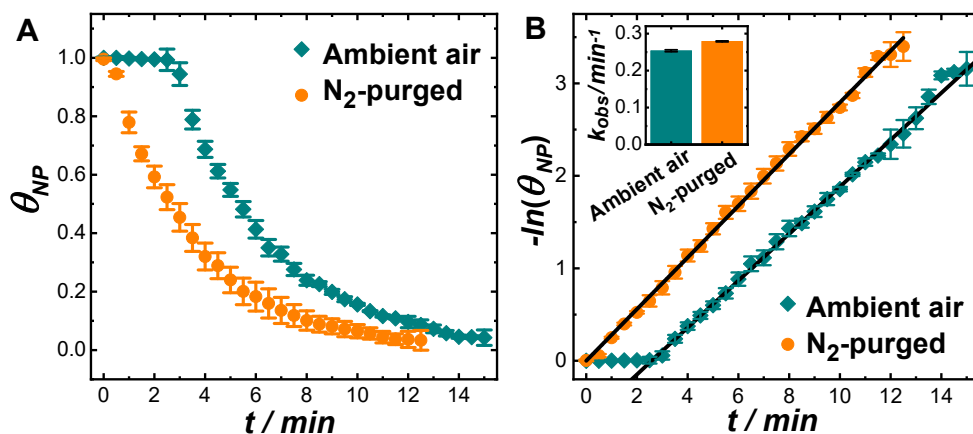


Figure S20. Temporal evolution of (A) θ_{NP} and (B) $-\ln(\theta_{NP})$ during the catalytic reactions at room temperature after mixing AB with NP in the presence of PDA@Pt-2 nanocatalysts under ambient air and in an N_2 -purged solution. The initial concentrations of NP, AB, and KOH were $56 \mu\text{M}$, 5.6 mM , and 10 mM , respectively. The volume of colloidal PDA@Pt-2 nanocatalysts (containing $44.9 \mu\text{g mL}^{-1}$ PDA) added to the reactant mixtures was $30 \mu\text{L}$. The total volume of the reactant mixtures was 1.8 mL . The error bars represent the standard deviations obtained from three experimental runs under identical reaction conditions. The results of least squares curve fitting are shown as solid lines in panel B and the values of k_{obs} under ambient air and in the N_2 -purged solution were compared in the inset of panel B.

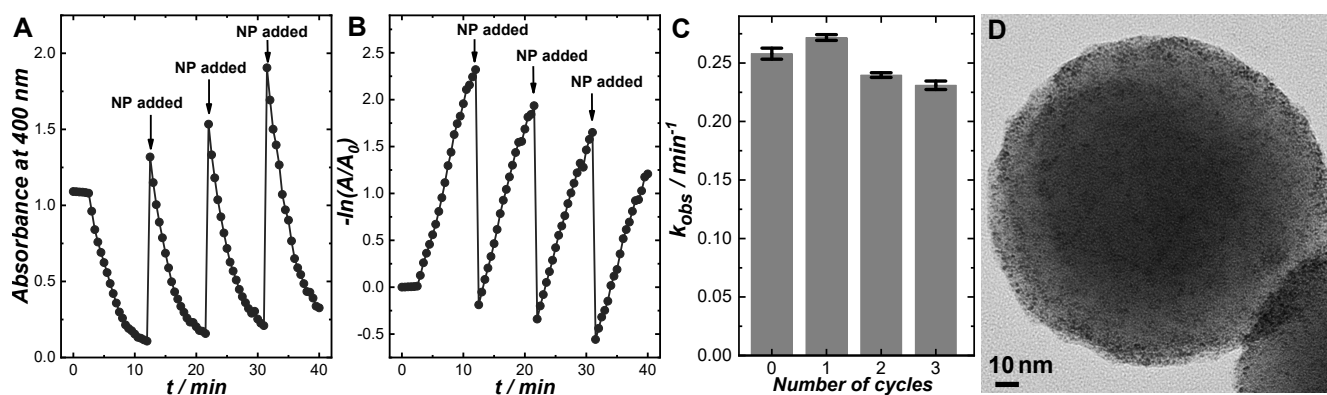


Figure S21. Temporal evolutions of (A) absorbance and (B) $-\ln(A/A_0)$ at λ of 400 nm after mixing AB with NP in the presence of PDA@Pt-2 (containing $1.35 \mu\text{g}$ PDA) during multiple reaction cycles. The initial concentrations of NP, AB, and KOH were $56 \mu\text{M}$, 5.6mM , and 10mM , respectively. The initial volume of the reactant mixtures was 1.8mL . After the majority of NP was hydrogenated, $10 \mu\text{L}$ of 10mM NP was added to start the second cycle of reactions. The following cycles were initiated by adding $10 \mu\text{L}$ of 10mM NP into the reactant mixtures each time and UV-vis absorption spectra were taken continuously to track the reaction progress in real time. The time spots at which additional NP was introduced were labeled with arrows in panels A and B. (C) Comparison of the apparent pseudo-first-order rate constant (k_{obs}) of each reaction cycle. The error bars represent the standard deviations of the least squares curve fitting. (D) TEM image of PDA@Pt-2 nanocatalysts collected after 4 reaction cycles.

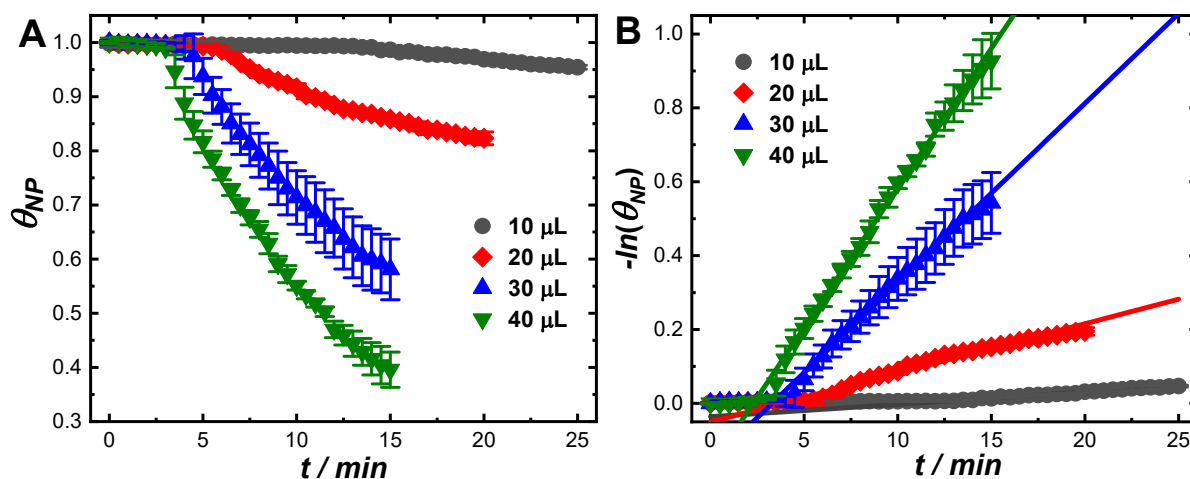


Figure S22. Temporal evolutions of (A) θ_{NP} and (B) $-\ln(\theta_{NP})$ during the catalytic reactions at room temperature after mixing AB with NP in the presence of various amounts of PDA@Pt-1 nanocatalysts. The initial concentrations of NP, AB, and KOH were $56 \mu\text{M}$, 5.6mM , and 10mM , respectively. The total volume of the reactant mixtures was kept at 1.8mL . The volumes of colloidal PDA@Pt-1 nanocatalysts (containing $44.9 \mu\text{g mL}^{-1}$ PDA) added to the reactant mixtures are labeled in the figure legends. The error bars in the panels represent the standard deviations obtained from three experimental runs under identical reaction conditions. The results of least squares curve fitting are shown as solid lines in panel B.

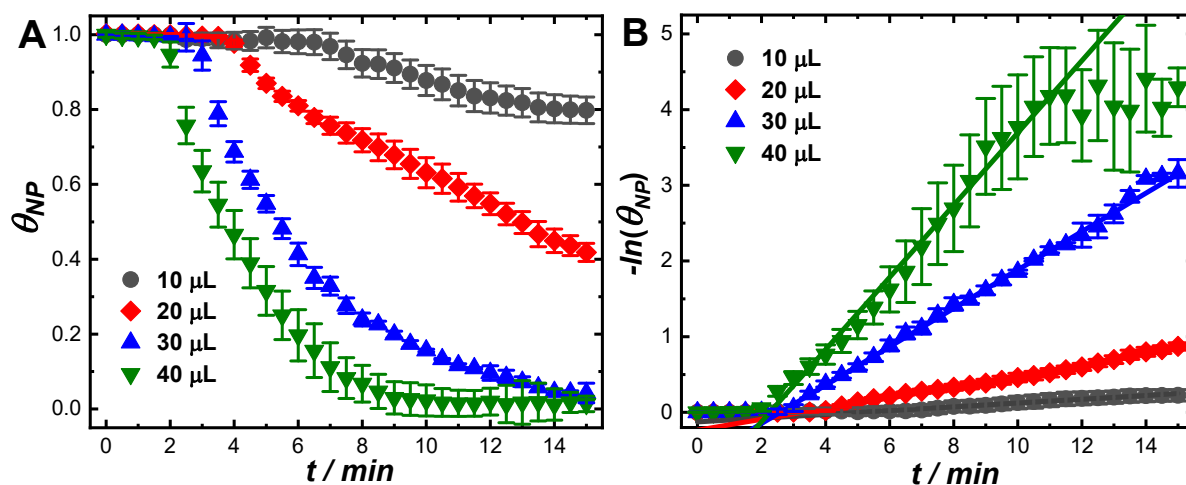


Figure S23. Temporal evolutions of (A) θ_{NP} and (B) $-\ln(\theta_{NP})$ during catalytic hydrogenation reactions at room temperature after mixing AB with NP in the presence of various amounts of PDA@Pt-2 nanocatalysts. The initial concentrations of NP, AB, and KOH were 56 μM , 5.6 mM, and 10 mM, respectively. The total volume of the reactant mixtures was kept at 1.8 mL. The volumes of colloidal PDA@Pt-2 nanocatalysts (containing 44.9 $\mu\text{g mL}^{-1}$ PDA) added to the reactant mixtures are labeled in the figure legends. The error bars in the panels represent the standard deviations obtained from three experimental runs under identical reaction conditions. The results of least squares curve fitting are shown as solid lines in panel B.

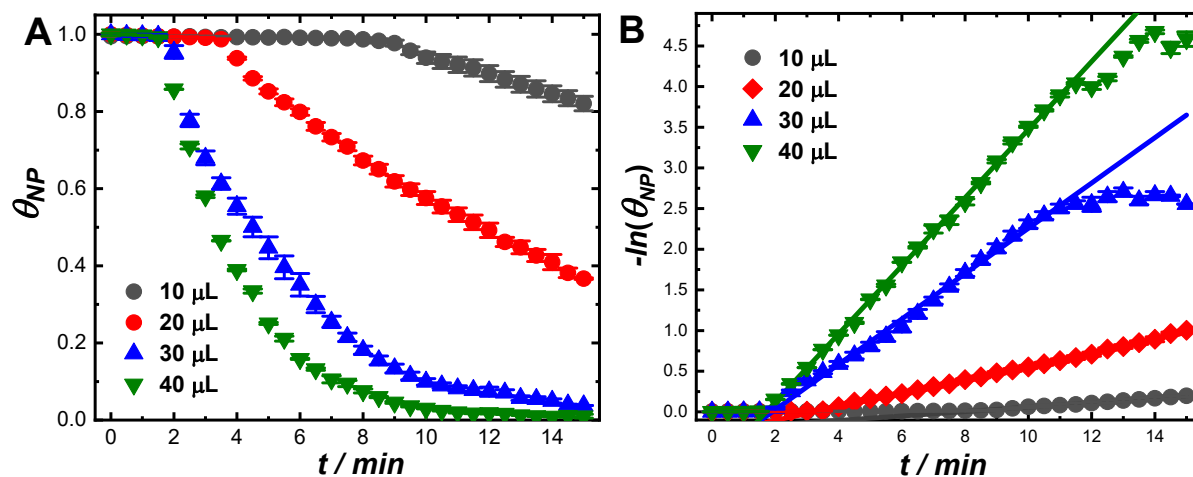


Figure S24. Temporal evolutions of (A) θ_{NP} and (B) $-\ln(\theta_{NP})$ during catalytic hydrogenation reactions at room temperature after mixing AB with NP in the presence of various amounts of PDA@Pt-3 nanocatalysts. The initial concentrations of NP, AB, and KOH were 56 μM , 5.6 mM, and 10 mM, respectively. The total volume of the reactant mixtures was kept at 1.8 mL. The volumes of colloidal PDA@Pt-3 nanocatalysts (containing 44.9 $\mu\text{g mL}^{-1}$ PDA) added to the reactant mixtures are labeled in the figure legends. The error bars in the panels represent the standard deviations obtained from three experimental runs under identical reaction conditions. The results of least squares curve fitting are shown as solid lines in panel B.

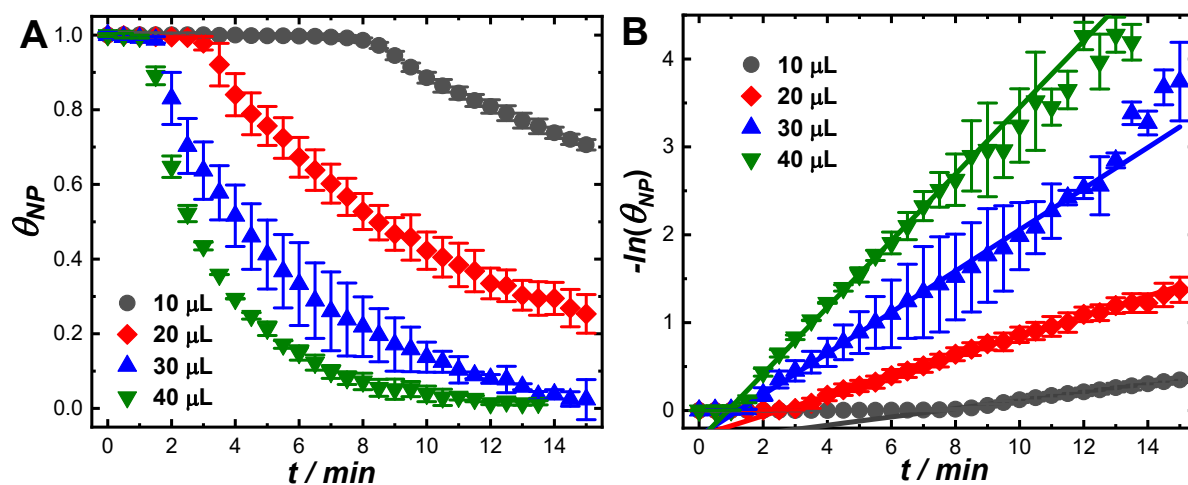


Figure S25. Temporal evolutions of (A) θ_{NP} and (B) $-\ln(\theta_{NP})$ during catalytic hydrogenation reactions at room temperature after mixing AB with NP in the presence of various amounts of PDA@Pt-4 nanocatalysts. The initial concentrations of NP, AB, and KOH were 56 μM , 5.6 mM, and 10 mM, respectively. The total volume of the reactant mixtures was kept at 1.8 mL. The volumes of colloidal PDA@Pt-4 nanocatalysts (containing 44.9 $\mu\text{g mL}^{-1}$ PDA) added to the reactant mixtures are labeled in the figure legends. The error bars in the panels represent the standard deviations obtained from three experimental runs under identical reaction conditions. The results of least squares curve fitting are shown as solid lines in panel B.

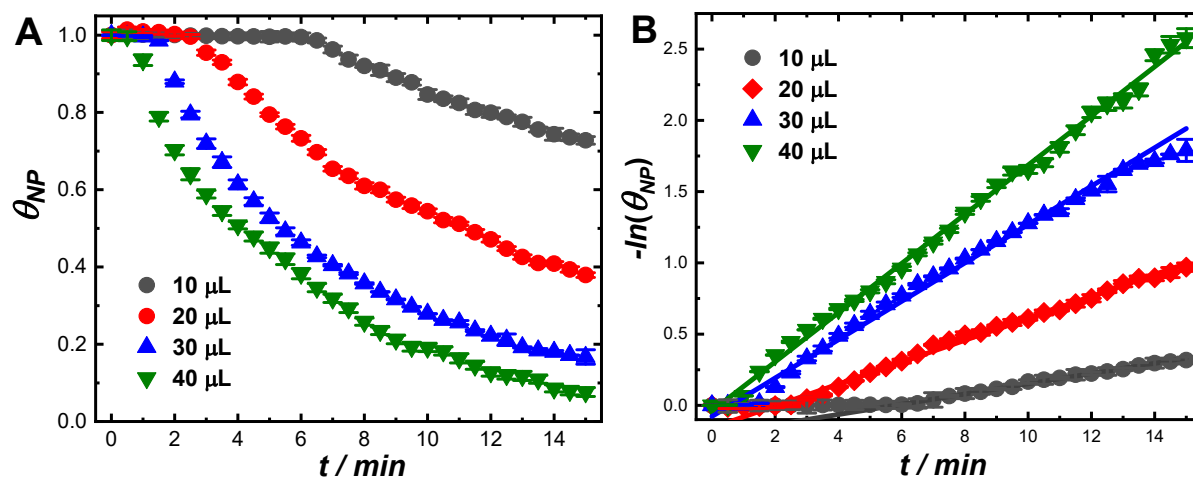


Figure S26. Temporal evolutions of (A) θ_{NP} and (B) $-\ln(\theta_{NP})$ during catalytic hydrogenation reactions at room temperature after mixing AB with NP in the presence of various amounts of PDA@Pt-5 nanocatalysts. The initial concentrations of NP, AB, and KOH were 56 μM , 5.6 mM, and 10 mM, respectively. The total volume of the reactant mixtures was kept at 1.8 mL. The volumes of colloidal PDA@Pt-5 nanocatalysts (containing 44.9 $\mu\text{g mL}^{-1}$ PDA) added to the reactant mixtures are labeled in the figure legends. The error bars in the panels represent the standard deviations obtained from three experimental runs under identical reaction conditions. The results of least squares curve fitting are shown as solid lines in panel B.

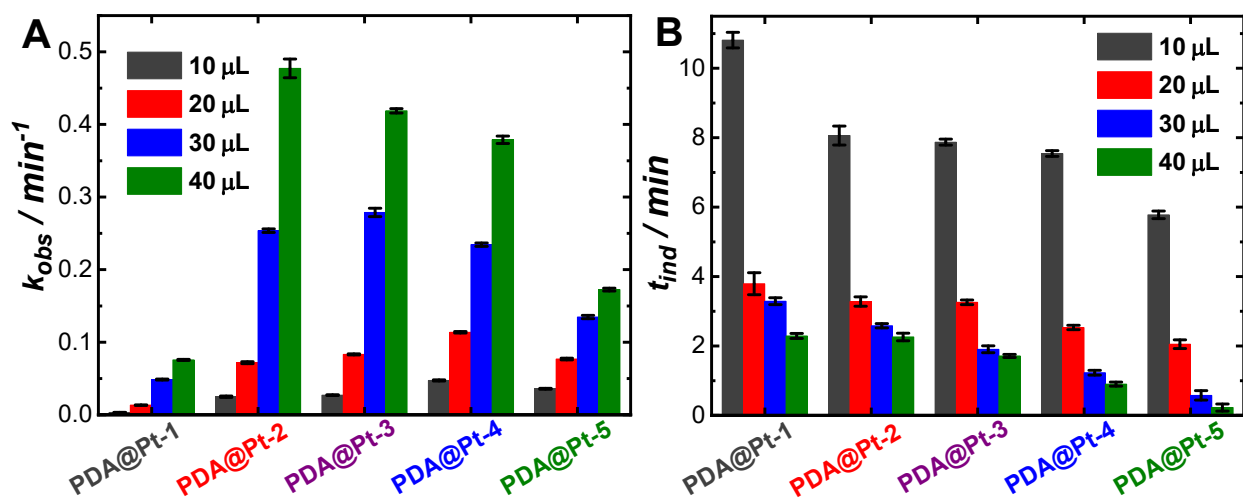


Figure S27. Comparison of (A) k_{obs} and (B) t_{ind} of the transfer hydrogenation reactions catalyzed by PDA@Pt-1, PDA@Pt-2, PDA@Pt-3, PDA@Pt-4, and PDA@Pt-5 nanocatalysts at various catalyst loading amounts. The initial concentrations of NP, AB, and KOH were 56 μM , 5.6 mM, and 10 mM, respectively. The total volume of the reactant mixtures was kept at 1.8 mL. The volumes of colloidal PDA@Pt nanocatalysts (containing 44.9 $\mu\text{g mL}^{-1}$ PDA) added to the reactant mixtures are labeled in the figure legends. The error bars represent the standard deviations of the least squares curve fitting.

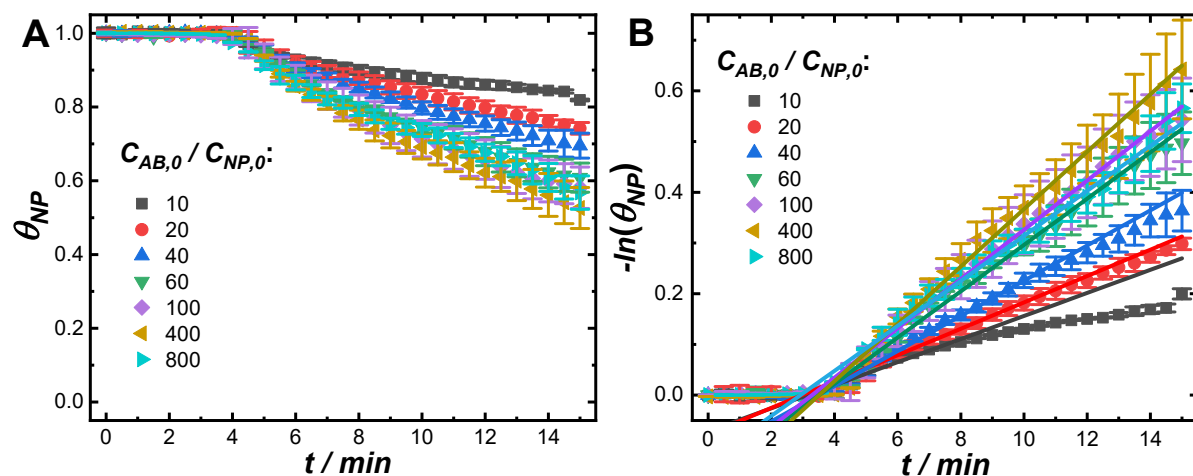


Figure S28. Temporal evolutions of (A) θ_{NP} and (B) $-\ln(\theta_{NP})$ during PDA@Pt-1-catalyzed transfer hydrogenation reactions at room temperature at various $C_{AB,0} / C_{NP,0}$ ratios. The initial concentrations of NP and KOH were 56 μM and 10 mM, respectively. The total volume of the reactant mixtures was kept at 1.8 mL. The PDA@Pt-1 nanocatalysts in the reaction mixtures contained 1.35 μg PDA. The error bars in the panels represent the standard deviations obtained from three experimental runs under identical reaction conditions. The results of least squares curve fitting are shown as solid lines in panel B.

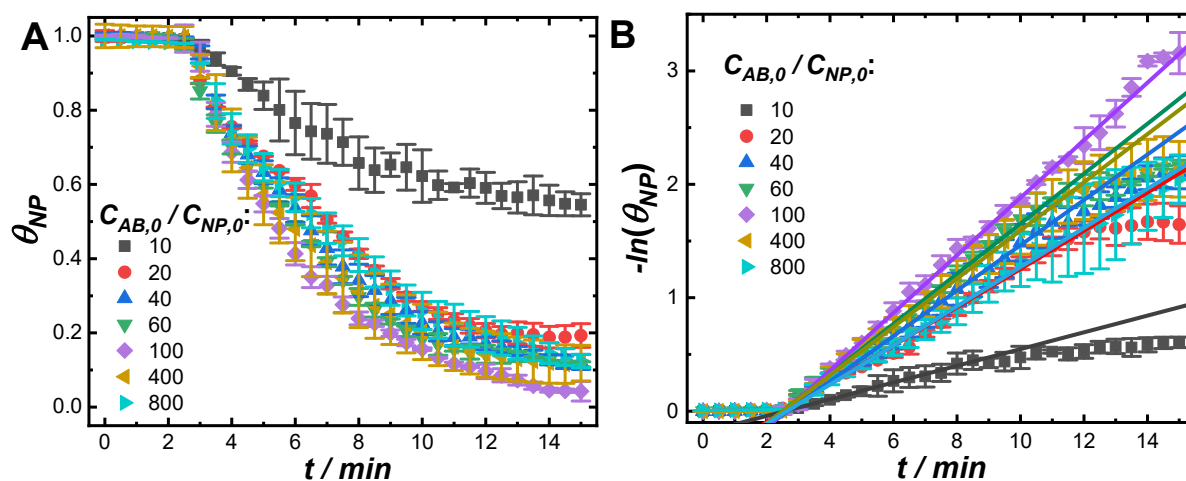


Figure S29. Temporal evolutions of (A) θ_{NP} and (B) $-\ln(\theta_{NP})$ during PDA@Pt-2-catalyzed transfer hydrogenation reactions at room temperature at various $C_{AB,0}/C_{NP,0}$ ratios. The initial concentrations of NP and KOH were $56 \mu\text{M}$ and 10 mM , respectively. The total volume of the reactant mixtures was kept at 1.8 mL . The PDA@Pt-2 nanocatalysts in the reaction mixtures contained $1.35 \mu\text{g}$ PDA. The error bars in the panels represent the standard deviations obtained from three experimental runs under identical reaction conditions. The results of least squares curve fitting are shown as solid lines in panel B.

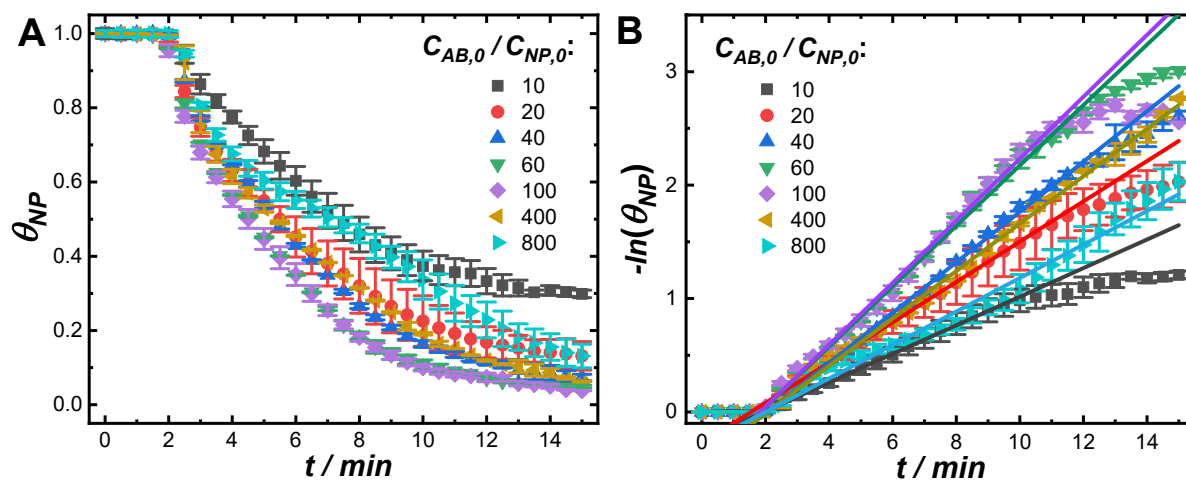


Figure S30. Temporal evolutions of (A) θ_{NP} and (B) $-\ln(\theta_{NP})$ during PDA@Pt-3-catalyzed transfer hydrogenation reactions at room temperature at various $C_{AB,0}/C_{NP,0}$ ratios. The initial concentrations of NP and KOH were $56 \mu\text{M}$ and 10 mM , respectively. The total volume of the reactant mixtures was kept at 1.8 mL . The PDA@Pt-3 nanocatalysts in the reaction mixtures contained $1.35 \mu\text{g}$ PDA. The error bars in the panels represent the standard deviations obtained from three experimental runs under identical reaction conditions. The results of least squares curve fitting are shown as solid lines in panel B.

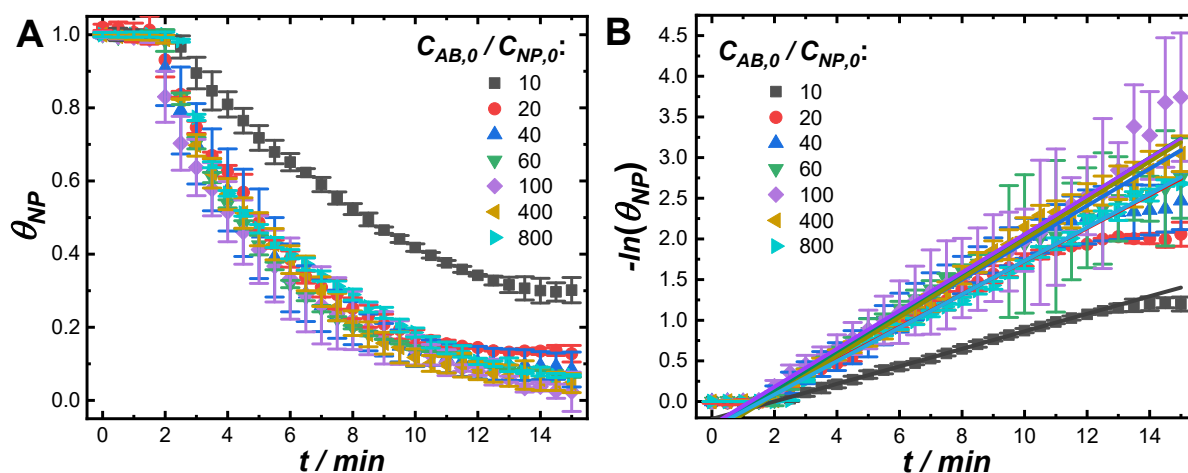


Figure S31. Temporal evolutions of (A) θ_{NP} and (B) $-\ln(\theta_{NP})$ during PDA@Pt-4-catalyzed transfer hydrogenation reactions at room temperature at various $C_{AB,0}/C_{NP,0}$ ratios. The initial concentrations of NP and KOH were $56 \mu\text{M}$ and 10 mM , respectively. The total volume of the reactant mixtures was kept at 1.8 mL . The PDA@Pt-4 nanocatalysts in the reaction mixtures contained $1.35 \mu\text{g}$ PDA. The error bars in the panels represent the standard deviations obtained from three experimental runs under identical reaction conditions. The results of least squares curve fitting are shown as solid lines in panel B.

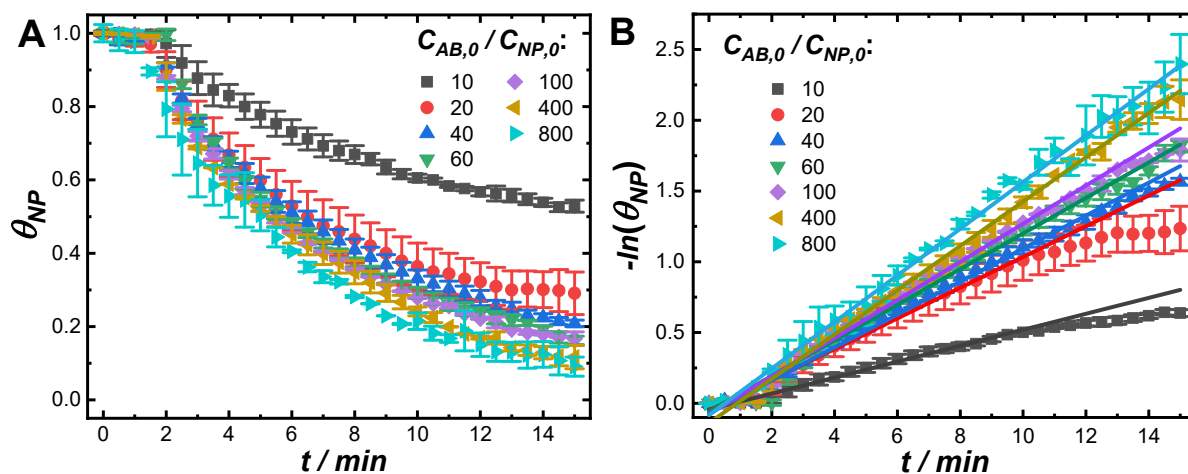


Figure S32. Temporal evolutions of (A) θ_{NP} and (B) $-\ln(\theta_{NP})$ during PDA@Pt-5-catalyzed transfer hydrogenation reactions at room temperature at various $C_{AB,0}/C_{NP,0}$ ratios. The initial concentrations of NP and KOH were $56 \mu\text{M}$ and 10 mM , respectively. The total volume of the reactant mixtures was kept at 1.8 mL . The PDA@Pt-5 nanocatalysts in the reaction mixtures contained $1.35 \mu\text{g}$ PDA. The error bars in the panels represent the standard deviations obtained from three experimental runs under identical reaction conditions. The results of least squares curve fitting are shown as solid lines in panel B.

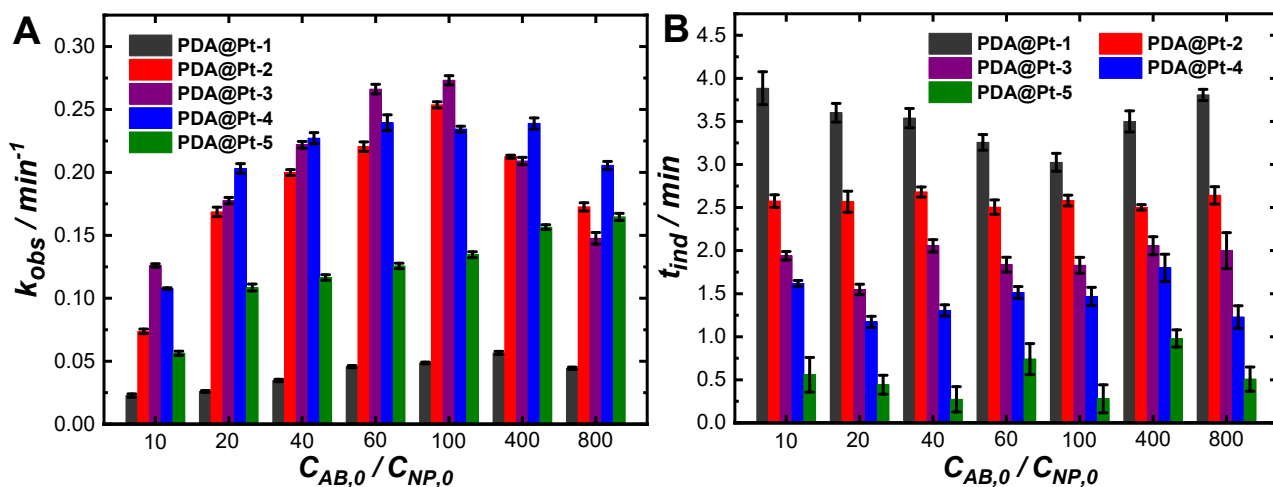


Figure S33. Comparison of (A) k_{obs} and (B) t_{ind} of the transfer hydrogenation reactions catalyzed by PDA@Pt-1, PDA@Pt-2, PDA@Pt-3, PDA@Pt-4, and PDA@Pt-5 nanocatalysts at $C_{AB,0}/C_{NP,0}$ ratios. The initial concentrations of NP and KOH were 56 μM and 10 mM, respectively. The total volume of the reactant mixtures was kept at 1.8 mL. The particle concentrations of various PDA@Pt nanocatalysts were kept the same, containing 1.35 μg PDA in each reaction mixture. The error bars represent the standard deviations of the least squares curve fitting.

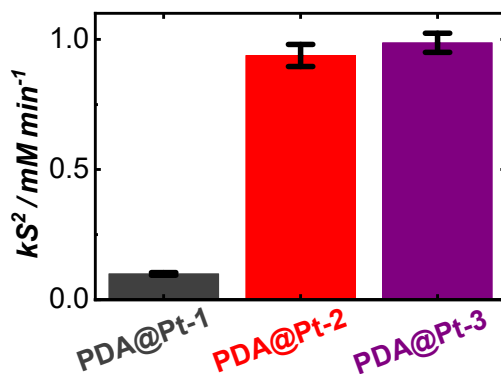


Figure S34. kS^2 values of PDA@Pt-1, PDA@Pt-2, PDA@Pt-3 obtained through curve fitting.

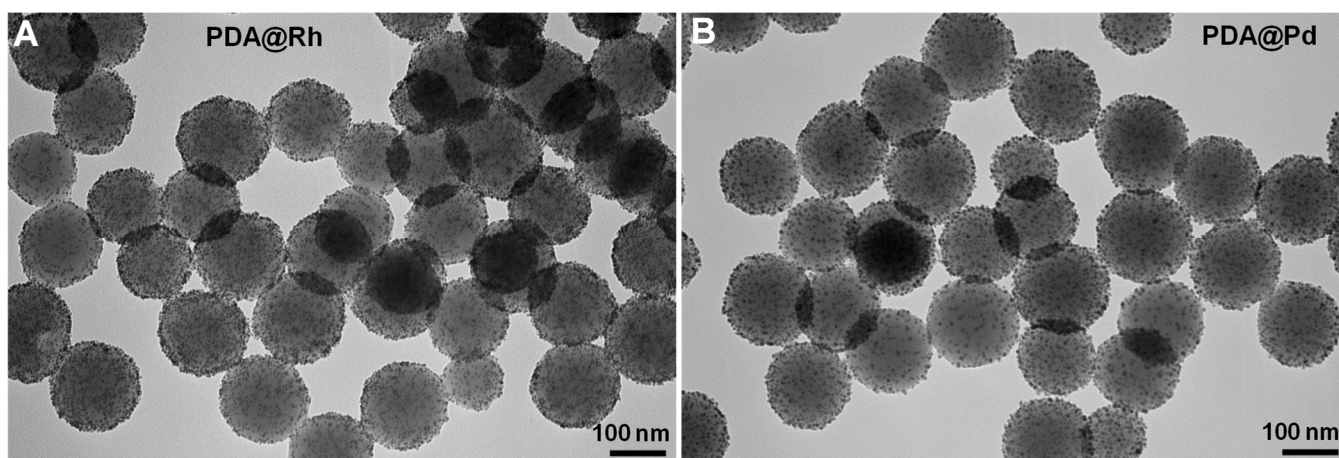


Figure S35. TEM images of (A) PDA-supported Rh (PDA@Rh) and (B) PDA-supported Pd (PDA@Pd) nanocatalysts. The detailed procedures for the nanoparticle synthesis were described in Section S1.8 in the Supporting Information.

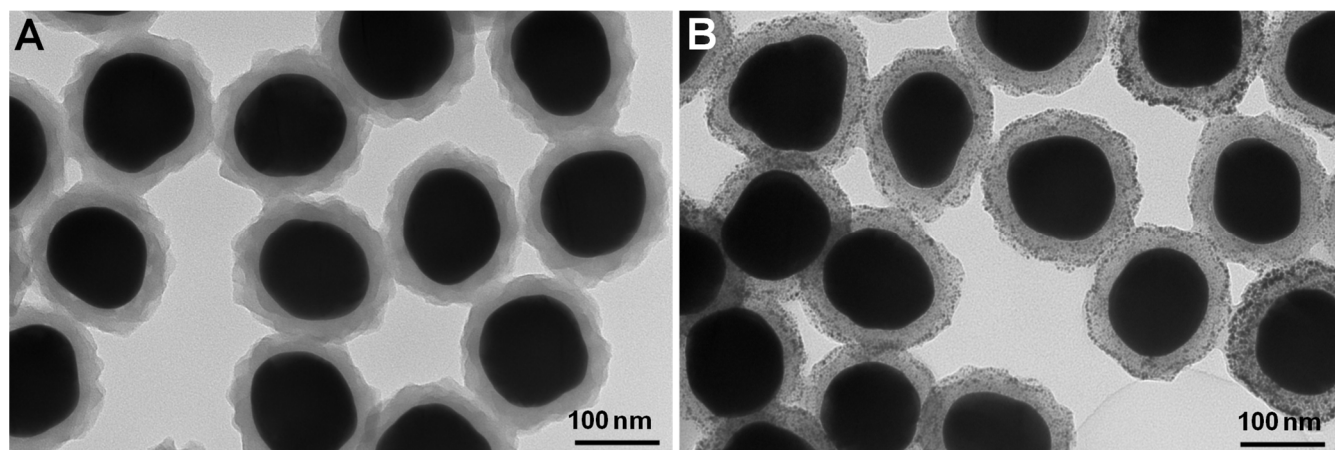


Figure S36. TEM images of (A) Au@PDA core-shell nanoparticles and (B) Pt nanocatalysts on Au@PDA core-shell supports. The detailed procedures for the nanoparticle synthesis were described in Section S1.9 in the Supporting Information.

S3. References for Supplementary Information

1. W. B. Qiang, W. Li, X. Q. Li, X. Chen and D. K. Xu, *Chem. Sci.*, 2014, **5**, 3018-3024.
2. S. E. Skrabalak, B. J. Wiley, M. Kim, E. V. Formo and Y. N. Xia, *Nano Lett.*, 2008, **8**, 2077-2081.
3. G. G. Li, Z. X. Wang, D. A. Blom and H. Wang, *ACS Appl. Mater. Interfaces*, 2019, **11**, 23482-23494.
4. E. P. Lee, Z. M. Peng, D. M. Cate, H. Yang, C. T. Campbell and Y. N. Xia, *J. Am. Chem. Soc.*, 2007, **129**, 10634-10635.
5. H. Goksu, S. F. Ho, O. Metin, K. Korkmaz, A. M. Garcia, M. S. Gultekin and S. H. Sun, *ACS Catal.*, 2014, **4**, 1777-1782.
6. L. C. Sun, Q. F. Zhang, G. G. Li, E. Villarreal, X. Q. Fu and H. Wang, *ACS Nano*, 2017, **11**, 3213-3228.
7. Q. F. Zhang, Y. D. Zhou, E. Villarreal, Y. Lin, S. L. Zou and H. Wang, *Nano Lett.*, 2015, **15**, 4161-4169.
8. X. Wang, D. P. Liu, S. Y. Song and H. J. Zhang, *J. Am. Chem. Soc.*, 2013, **135**, 15864-15872.
9. P. N. Zhang, Y. J. Li, D. Y. Wang and H. B. Xia, *Part. Part. Syst. Character.*, 2016, **33**, 924-932.